Journal of Advanced Electrochemical Storage

ISSN (Online): 3139-7190

Indexed in www.pubj.org



Investigation of Structural, Magnetic and Surface analysis of Sr Doped $BaFe_{12}O_{19}$ via Co-precipitation Method

Vadivelan Subramaniyan[1,*], Sowmiya Srinivasan[2]

[1]*Department of Physics, Karpaga Vinayaga College of Engineering and Technology, Karpaga Vinayaga Educational Lore for Learning (Deemed to be University), GST Road, Chinna Kolambakkam, Chengalpattu, Tamil Nadu, 603 308, India.*

[2]*Department of Physics, SRM Valliammai Engineering College, Kattankulathur, 603203, Tamil Nadu, India.*

*Corresponding author: starvel30@gmail.com

DOI: https://doi.org/10.67977/jaes.vol.2.issue1.4

J. Adv. Electro. Storage 2(1) 2026 150−156

Keywords:
$Ba_{1-x}Sr_xFe1_2O19$; Barium hexaferrite; Co-precipitation Method; X-ray diffraction; Magnetic and Surface analysis.

Received 9th March 2026
Published 11th May 2026

Licensed under CC-BY 4.0

ABSTRACT: Tunable structural, thermal, surface, and magnetic properties, strontium-doped barium hexaferrite ($Ba_{1-x}Sr_xFe_{12}O_{19}$) nanoparticles have garnered significant interest as potential candidates for cutting-edge technological applications. To examine the impact of Sr^{2+} substitution on the physicochemical properties of strontium-substituted barium ferrite nanoparticles, a controlled production method was used. Thermogravimetric analysis (TGA) was used to assess thermal stability and decomposition behavior, while X-ray diffraction (XRD) was used to study the structural characteristics and phase formation. The ferrite framework was verified and distinctive metal–oxygen vibrational modes were identified using Fourier transform infrared spectroscopy (FTIR). The elemental composition and Brunauer-Emmett-Teller (BET) analysis was used to calculate specific surface area, pore volume, and pore-size distribution. Additionally, morphology of the prepared samples was analyzed using SEM characterization and saturation magnetization, remanent magnetization, coercivity, and magnetic behavior were assessed using vibrating sample magnetometry (VSM). The structure-property correlations of strontium-doped barium ferrite and its prospective appropriateness for high-performance magnetic, electrical, and energy-related applications are revealed by this thorough analysis.

1. INTRODUCTION

The substance barium ferrite (BaFe) has a high packing density and is strongly magnetic. Ferrite compounds are being utilized in magnetic tapes, speakers, and card strips. Long-term data storage devices in particular are successfully located. These materials have resistance to oxidation, corrosion, and temperature. The material has demonstrated resistance to various environmental stressors, such as corrosion and dampness. Ferrites cannot be further oxidized since they have previously been oxidized. Ferrites are extremely resistant to corrosion for this reason [1-3]. Additionally, barium ferrite demonstrated resistance to thermal demagnetization, another problem that frequently arises during long-term storage. The coercivity value significantly increased as the temperature rose. It is more resistant to thermal demagnetization as a result of this action. Because of this

How to cite this article: Vadivelan Subramaniyan, S. Sowmiya. (2026). Investigation of Structural, Magnetic and Surface analysis of Sr Doped $BaFe_{12}O_{19}$ via Co-precipitation Method, Journal of Advanced Electrochemical Storage, 2(1), 150–156. https://doi.org/10.67977/vol.2.issue1.4

feature, barium ferrite is frequently used in loudspeaker applications as well as motor and generator designs. Ferrite magnets are brittle, demonstrating their ceramic properties, and they are very good insulators that prevent any electrical current from passing through them [4-5]. Additionally, ferrite magnets have outstanding machining qualities that enable the material to be machined in a variety of sizes and shapes. Barium ferrites are sturdy ceramics that are often resistant to corrosion and moisture. Barium ferrite is a highly useful substance utilized in numerous industrial domains. Applications for the material can be found all across the world, including magnetic stripe cards, permanent magnets, and recording devices such cassettes and other media [6–8]. The material's resilience allows it to be significantly reduced in size, increasing the packing density. The oxide has lately been replaced by barium ferrite, which provides much greater coercivity levels and makes the material magnetically hard, making the ferrite better for recording materials. These magnetic stripe cards and their readers are implanted, as was previously discussed. Generally magnets are made of barium ferrite. By pressing powdered barium ferrite into a mold and heating it until it fuses together, a process known as sintering allows the materials to be shaped into nearly any size and shape. The barium ferrite maintains its magnetic characteristics when solidifying into a block [9-10]. Because of their exceptional resistance to demagnetization, the magnets can be used in speaker units for a very long time. As the materials' surface area increases, so does the packing density of barium ferrite [11–12]. This feature makes it possible to record additional data in the materials. Magnetic materials will boost the barium ferrite materials' storage capacity with various doped percentage. Strontium can be utilized as a doped material in different percentages since it is more stable and magnetic. For $Fe^{2+/3+}$, the divalent transition metals are $Co^{2+/3+}$, $Ni^{2+/3+}$, and $Sr^{2+/3+}$. Because of their comparable ionic radius and electronic structures, they are often employed [13–14]. The synthesis method and structure of this chemical determine its magnetic and dielectric properties. The co-precipitation method, however, is a superior method for analyzing the compound's characteristics

2. Experimental

2.1. Chemicals

Barium hexaferrite doped with strontium is made using the co-precipitation process at different doping percentages. The necessary ratios of barium nitrite, iron nitrate, strontium nitrate, citric acid, and NH_3 were added to the distilled water. The process is controlled by ammonium hydroxide.

2.2. *Material and methods*

The strontium doped barium hexaferrite is prepared by co-precipitation method with various doping percentage. The raw materials of the barium nitrite, iron nitrate, strontium nitrate, citric acid and NH_3 were taken in the required ratio with the distilled water. The ammonium hydroxide is used to regulate the synthesized process. The mixtures of the raw materials were stirrer at 80°C up to 2 hrs. The prepared solution is washed 4 or 5 times with distilled water and ethanol separately because of the dust particles are removed. Finally, strontium doped barium hexaferrite is prepared in the form of powder particles. The prepared powder samples are involved the sintering process at the temperature 1000°C up to 5 hrs. After sintering process, the sintered powder samples are concerned the grinding process up to nanoparticle size.

3. RESULTS AND DISCUSSION

3.1. *X-ray diffraction (XRD) analysis*

The crystal structure, phase formation, crystallinity, and structural alterations of 1%, 2%, and 3% strontium-doped barium ferrite nanoparticles were examined using PANalytical X"pert PRO X-ray diffractometry using CuKα radiation between the region of 2θ=10-80° with a step scan of 0.02°/min Cell parameters were calculated and also refined using linear regression procedures applied to the measured peak positions of all major reflections up 90°. The JCPDS 78-0133 diffraction files were used to match the evolving phases [15-16]. The strong diffraction peaks of pure and strontium doped barium hexaferrite samples exhibit standard peaks at 2θ values corresponding to (114), (107) and (110) planes respectively. The hexagonal crystal structure of barium ferrite ($BaFe_{12}O_{19}$) is expected to be represented by distinctive peaks in the diffraction patterns. The creation of the ferrite phase can be verified by indexing the observed diffraction peaks to the corresponding crystallographic planes. Systematic changes in peak intensity, peak position, and full width at half maximum (FWHM) with increasing strontium concentration may be indicative of changes in microstructural features, lattice parameters, and crystallite size [17-19]. Due to variations in ionic radii, the substitution of Sr^{2+} ions at Ba^{2+} sites might alter the

lattice dimensions, which may have an impact on the crystallinity and structural stability of the produced nanoparticles and the Debye–Scherrer equation is

$$t = (k\lambda/\beta\cos\theta).$$

Where k=Scherrer constant (k=0.9), t= average size of the crystallite, λ=wavelength of radiation (λ=1.54056Å), β=full width half maximum of the diffraction peak at θ and θ=diffraction angle corresponds to the peak position measured in radian as shown in Figure.1.

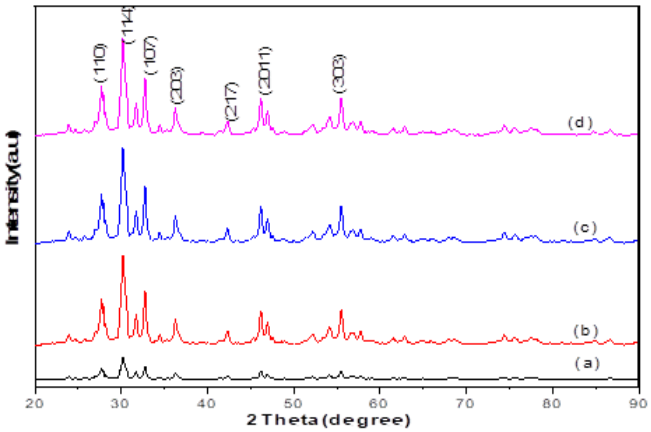

Figure 1. XRD pattern of the sample: (a) Pure barium ferrite (b) Sr 1%, (c) Sr 2% & (d) Sr 3%.

3.2. TGA/DTA analysis

The thermal stability, breakdown efficiency, and weight-loss properties of pure barium ferrite nanoparticles were examined using thermogravimetric analysis (TGA) as shown in Figure 2 [20–21]. TGA curves offer important insights into the synthetic materials thermal sensitivity across the chosen temperature range. In general, there are three different stages to the heat breakdown process. The removal of physically adsorbed moisture and leftover solvents is mostly responsible for the initial weight loss at lower temperatures (30–200 °C). The breakdown of organic molecules, nitrate leftovers, and intermediate precursor materials occurs during the second stage (210–515 °C). The removal of any remaining hydroxyl groups and the advancement of the ferrite crystalline phase are linked to the third stage (515–920 °C) [20–21]. The pure barium ferrite nanoparticles variation in weight-loss percentage and thermal decomposition behavior may reflect differences in precursor composition and segment development. From the curve nearly stable weight observed at higher temperatures indicates the oxide formation is thermally stable [22-24]. This analysis establishes the thermal stability and suitable heat-treatment conditions of the synthesized nanoparticles, associate their potential for high-temperature magnetic applications.

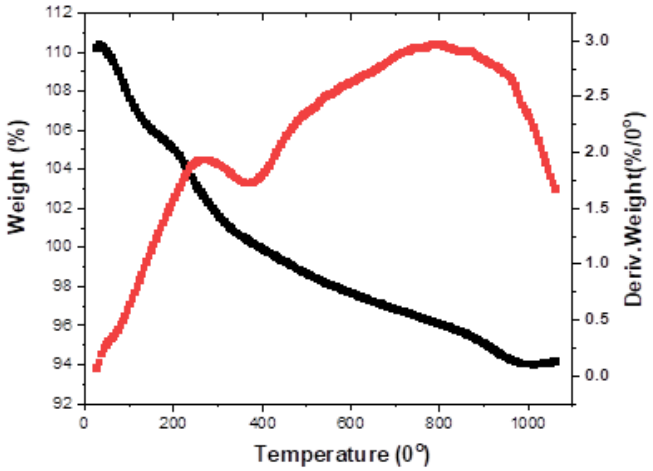

Figure. 2. TG/DTA analysis of the pure barium ferrite nanoparticles.

3.3. Fourier transforms infrared spectroscopy (FT-IR) analysis

Fourier transform infrared (FTIR) spectroscopy was active to investigate the functional groups, chemical bonding, and metal–oxygen vibrational characteristics of pure and strontium doped barium ferrite nanoparticles. The FTIR spectra provide valuable information regarding the formation of the hexagonal M-type ferrite structure and the effect of Sr^{2+} combination on the local bonding environment [25-28]. The typical absorption bands generally observed in the 400–700 cm^{-1} region is accredited to metal–oxygen (Fe–O) stretching vibrations as shown in Figure 3. The higher-frequency absorption band, typically around 550–600 cm^{-1}, is associated with tetrahedral metal–oxygen vibrations, while the lower-frequency band around 400–450 cm^{-1} matches to octahedral metal–oxygen vibrations. These bands are confirming the formation of the pure and doped ferrite structure [29]. The pure and strontium doped barium ferrite nanoparticles absorption intensity, bandwidth, and peak positions may arise from changes in metal–oxygen bond lengths, lattice alteration, and local force constants. C=C and C-C bands are identified 2300-2350 cm^{-1} and 2900-3010 cm^{-1} respectively. A broad absorption band around 3200–3600 cm^{-1} may indicate O–H stretching vibrations, while a band near 1600–1650 cm^{-1} can be associated with H–O–H bending vibrations of adsorbed moisture [30].

From the analysis it helps as to establish the structural integrity and bonding characteristics of the synthesized nanoparticles.

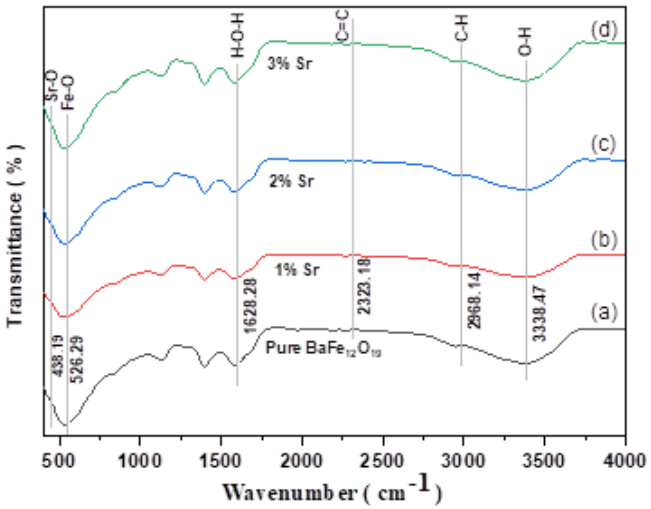

Figure. 3. FTIR pattern of the sample: (a) Pure barium ferrite (b) Sr 1%, (c) Sr 2% & (d) Sr 3%.

3.4. Scanning electron microscopy (SEM) analysis

Scanning electron microscopy (SEM) was active to investigate the surface morphology, particle distribution, grain structure, and collection behavior of pure and strontium doped (1%) barium ferrite nanoparticles. The SEM micrographs provide valuable information about the influence of Sr^{2+} assimilation on the morphological growth of the synthesized ferrite materials as shown in Figure 4. In this analysis exhibit hexagonal platelet-like, spherical, or irregular morphologies depending on the synthesis and calcination environments. Variations in particle size and collection with increasing strontium concentration may be associated with changes in grain growth and interparticle magnetic interactions [31-32]. The morphological characteristics complement the structural findings obtained from XRD analysis and helps to establish the composition dependent properties of the prepared pure and dope ferrite nanoparticles and SEM supports the evaluation of their potential for advanced magnetic applications.

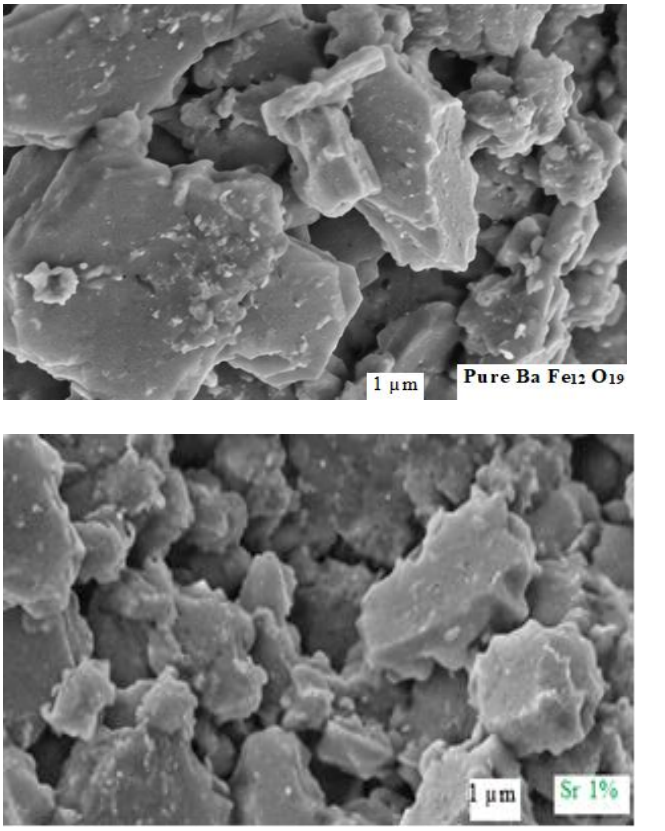

Figure. 4. SEM image of the sample: Pure and strontium doped barium ferrite.

3.5. BET analysis

The Brunauer–Emmett–Teller (BET) method was used to examine the specific surface area, pore volume, and average pore diameter of strontium-doped barium ferrite nanoparticles. The surface properties and porous structure of the synthesized material are revealed by the nitrogen adsorption–desorption isotherm as shown in Figure 5. Depending on the outcomes of the experiment, the observed adsorption behavior and hysteresis loop may reveal mesoporous properties [33-34]. Particle size, shape, and level of agglomeration are all related to the BET surface area. The accessible surface area and pore structure may change because of strontium substitution's effects on crystallite development and particle packing. Understanding the material's potential in magnetic, catalytic, and energy-related applications depends on these textural characteristics. Figure: BET nitrogen adsorption–desorption isotherm and pore-size distribution of strontium-doped barium ferrite nanoparticles.

The specific surface area, pore volume, and porous properties of synthetic barium ferrite nanoparticles are examined using the Brunauer–

Emmett–Teller (BET) methodology. The material's pore distribution and surface contact are shown by the nitrogen adsorption–desorption isotherm. The isotherm's hysteresis loop suggests capillary condensation inside the pores, indicating the presence of mesoporous properties. While the pore size distribution is often assessed using the BJH method, the BET surface area is computed from the linear section of the adsorption data [35-37]. The adsorption behavior and interfacial characteristics of barium ferrite are strongly influenced by the surface area and pore structure. These features are crucial for comprehending its possible uses in energy-related electronics, gas sensing, magnetic materials, and catalysis.

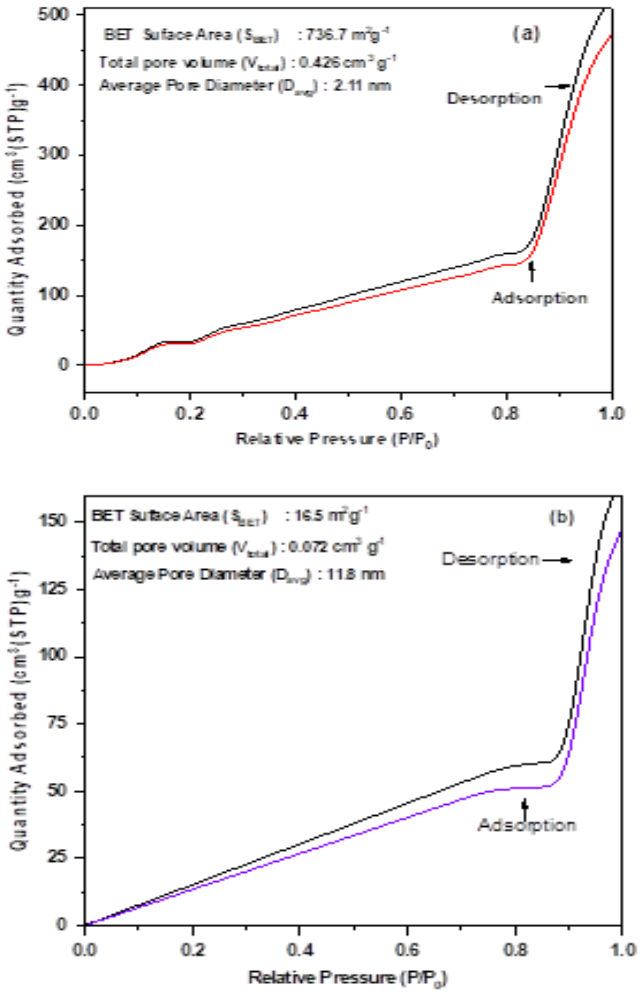

Figure. 5. BET analysis: (a) Pure barium ferrite and (b) Strontium (1%) doped barium ferrite.

3.6. Vibrating sample magnetometer (VSM) analysis

The magnetic behaviour of pure barium and strontium-doped ferrite nanoparticles at ambient temperature was examined using vibrating sample magnetometry (VSM). Magnetic hysteresis (M–H) loops as shown in Figure 6 were used to assess the magnetic properties, yielding crucial data regarding saturation magnetization (Ms), remanent magnetization (Mr), coercivity (Hc), and squareness ratio (SQR) [38-40]. It is anticipated that the observed hysteresis loops will show that the produced strontium doped barium ferrite nanoparticles. The ferrite system's exchange coupling, magneto crystalline anisotropy, and magnetic interactions are all affected by the addition of Sr^{2+} ions to the Ba^{2+} lattice sites.

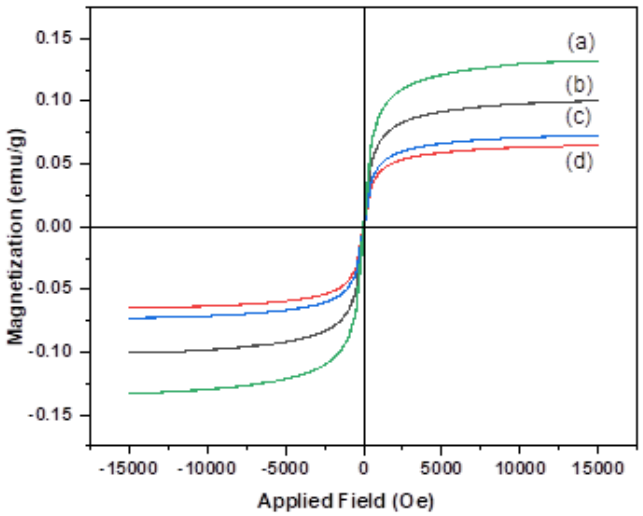

Figure 6 Hysteresis curve: (a) Pure barium ferrite (b) Sr 1% (c) Sr 2% Sr 3%.

Table 1: Magnetic parameters of pure barium and strontium-doped ferrite nanoparticles.

Sample	(Ms) (emu/g)	(Mr) (emu/g)	Squareness (Mr/Ms)	(Hc) (Oe)
Pure	0.130	0.013	0.101	135.658
1%	0.100	0.032	0.327	136.548
2%	0.072	0.008	0.112	137.154
3%	0.064	0.002	0.041	138.754

Changes in the Fe^{3+} magnetic sub lattice, particle size, and spin arrangement may be linked to variations in saturation magnetization with increasing strontium concentration. Similarly, changes in morphology, magnetic domain structure, and magneto crystalline anisotropy can all be linked to variations in coercivity. When the applied magnetic field is removed, the residual magnetic moment is represented by the remanent magnetization, and the magnetic reversal behaviour is shown by the squareness ratio (Mr/Ms) in

Table 1 [41-43]. Strontium substitution has been shown to considerably alter the saturation magnetization and coercivity of barium ferrite materials in earlier studies. From this analysis offers a thorough comprehension of the composition-dependent magnetic properties of the produced nanoparticles. Their applicability for permanent magnets, magnetic recording, electromagnetic devices, and advanced magnetic storage applications may be improved by the optimal strontium content.

4. CONCLUSION

The characterization of pure and strontium-doped barium ferrite nanoparticles for sophisticated magnetic applications is successfully demonstrated in this study. Using X-ray diffraction (XRD) they were identify the structure of the sample is hexagonal. From the FTIR the Metal–oxygen bonding, elemental chemical states are clarified and functional groups are identified. Using BET analysis, the surface area is decreased with increased the doped percentage of strontium as mentioned in the figure. VSM measurements determine how strontium concentration changes saturation magnetization, remanent magnetization and coercivity are calculated and tabulated. From the calculation the squareness values are decreased (0.327 -0.041) with increasing the doped ratio of strontium and increasing the coercivity (135.658 Oe -138.754 Oe) value of the strontium doped barium ferrite nanoparticles. It is anticipated that the three compositions will be compared to determine the ideal strontium content with desired structural and magnetic properties. The major application of this work is to increase the storage capacity of the prepared samples. This method is graceful method to understand the good result with low cost. In these nanoparticles are used in high-frequency technical applications, permanent magnets, magnetic recording, and electromagnetic devices.

References

1. N. Raghuram, T. Subba Rao, K.C.B. Naidu, Investigations on functional properties of hydrothermally synthesized $Ba_{1-x}Sr_xFe_{12}O_{19}$ (x = 0.0–0.8) nanoparticles, Mater. Sci. Semicond. Process. 94 (2019) 136–150. https://doi.org/10.1016/j.mssp.2019.01.037.
2. N. Raghuram, T. Subba Rao, K.C.B. Naidu, Magnetic properties of hydrothermally synthesized $Ba_{1-x}Sr_xFe_{12}O_{19}$ (x = 0.0–0.8) nanomaterials, Appl. Phys. A 125 (2019) 839. https://doi.org/10.1007/s00339-019-3143-2.
3. A.Y. Mironovich, V.G. Kostishin, R.I. Shakirzyanov, A.A. Mukabenov, S.A. Melnikov, A.I. Ril, H.I. Al-Khafaji, Effect of the Fe/Ba and Fe/Sr ratios on the phase composition, dielectric properties and magnetic characteristics of M-type hexaferrites prepared by the hydrothermal method, J. Solid State Chem. 316 (2022) 123625. https://doi.org/10.1016/j.jssc.2022.123625.
4. Y. Jing, L. Jia, Y. Zheng, H. Zhang, Hydrothermal synthesis and competitive growth of flake-like M-type strontium hexaferrite, RSC Adv. 9 (2019) 33388–33394. https://doi.org/10.1039/C9RA06246G.
5. A.Y. Mironovich, V.G. Kostishin, H.I. Al-Khafaji, A.V. Timofeev, A.I. Ril, R.I. Shakirzyanov, E.S. Savchenko, S.E. Yamilov, Magnetic and structural properties of Co-substituted barium hexaferrite synthesized by hydrothermal method, J. Magn. Magn. Mater. 588 (2023) 171469. https://doi.org/10.1016/j.jmmm.2023.171469.
6. M. Naseem Shidaye, M. Rehman, Q. Abbas, S.K. Abbas, S.M. Ramay, M. Ali Shar, S. Atiq, Nano structural engineering of Ba-substituted Sr-hexaferrites for viable microwave absorbance and magnetic data storage, Physica B: Condens. Matter 666 (2023) 415125. https://doi.org/10.1016/j.physb.2023.415125.
7. Himanshi, R. Jasrotia, J. Prakash, R. Verma, P. Thakur, A. Kandwal, F. Wan, A. Thakur, Synthesis, characterization, and applications of doped barium hexaferrites: A review, Physica B: Condens. Matter 667 (2023) 415202. https://doi.org/10.1016/j.physb.2023.415202.
8. A. Gupta, P.K. Roy, Improved strontium hexaferrites: An overview of current progress in synthesis, properties, and applications, Mater. Sci. Eng. B (2024) 117458. https://doi.org/10.1016/j.mseb.2024.117458.
9. S.K. Yadav, D.P. Pabba, A. Soosairaj, K. Divya, A.A. Arunmozhi, L.R. Asirvatham, V.S. Manikandan, Study on the structural, magnetic, and magnetodielectric properties of M-type $BaFe_{12}O_{19}$ and $SrFe_{12}O_{19}$ hexaferrite nanoparticles, Surfaces and Interfaces (2024) 104956.
10. P.D. Mhase, V.C. Pujari, S.E. Shirsath, A.V. Fulari, S.S. Jadhav, C.V. Ramana, S.M. Patange, Advances in M-type hexaferrites: A review tailoring structural, magnetic, and microwave absorption properties for emerging technologies, Coord. Chem. Rev. 541 (2025) 216825. https://doi.org/10.1016/j.ccr.2025.216825.

11. W.M. Matran, M. Mustapha, M.F. Nor, The influences of additives in M-type (Ba and Sr) hexaferrites' microstructure, sintering and magnetic properties: A review, Mater. Today: Proc. (2024) 78–83. https://doi.org/10.1016/j.matpr.2023.11.037.
12. J. Smit, H.P.J. Wijn, Ferrites, Philips Technical Library, Eindhoven, 1959.
13. R.C. Pullar, Hexagonal ferrites: A review of the synthesis, properties and applications of hexaferrite ceramics, Prog. Mater. Sci. 57 (2012) 1191–1334. https://doi.org/10.1016/j.pmatsci.2012.04.001.
14. B.D. Cullity, S.R. Stock, Elements of X-Ray Diffraction, 3rd ed., Prentice Hall, New Jersey, 2001.
15. A. R. West, Solid State Chemistry and Its Applications, 2nd ed., Wiley, Chichester, 2014.
16. H. Klug, L. Alexander, X-Ray Diffraction Procedures for Polycrystalline and Amorphous Materials, 2nd ed., Wiley, New York, 1974.
17. P. Scherrer, Bestimmung der Größe und der inneren Struktur von Kolloidteilchen mittels Röntgenstrahlen, Nachr. Ges. Wiss. Göttingen (1918) 98–100.
18. G.K. Williamson, W.H. Hall, X-ray line broadening from filed aluminium and wolfram, Acta Metall. 1 (1953) 22–31. https://doi.org/10.1016/0001-6160(53)90006-6.
19. W.W. Wendlandt, Thermal Analysis, 3rd ed., Wiley, New York, 1986.
20. P.J. Haines, Principles of Thermal Analysis and Calorimetry, Royal Society of Chemistry, Cambridge, 2002.
21. M.E. Brown, Introduction to Thermal Analysis: Techniques and Applications, 2nd ed., Kluwer Academic Publishers, Dordrecht, 2001.
22. H. K. D. H. Bhadeshia, Thermal analysis and its applications in materials characterization, relevant background reference for thermal characterization.
23. S. Brunauer, P.H. Emmett, E. Teller, Adsorption of gases in multimolecular layers, J. Am. Chem. Soc. 60 (1938) 309–319. https://doi.org/10.1021/ja01269a023.
24. E.P. Barrett, L.G. Joyner, P.P. Halenda, The determination of pore volume and area distributions in porous substances. I. Computations from nitrogen isotherms, J. Am. Chem. Soc. 73 (1951) 373–380. https://doi.org/10.1021/ja01145a126.
25. S. Lowell, J.E. Shields, M.A. Thomas, M. Thommes, Characterization of Porous Solids and Powders: Surface Area, Pore Size and Density, Springer, Dordrecht, 2004.
26. M. Thommes, K. Kaneko, A.V. Neimark, J.P. Olivier, F. Rodriguez-Reinoso, J. Rouquerol, K.S.W. Sing, Physisorption of gases, with special reference to the evaluation of surface area and pore size distribution (IUPAC Technical Report), Pure Appl. Chem. 87 (2015) 1051–1069. https://doi.org/10.1515/pac-2014-1117.
27. B.D. Cullity, C.D. Graham, Introduction to Magnetic Materials, 2nd ed., Wiley-IEEE Press, Hoboken, 2009.
28. R.M. Bozorth, Ferromagnetism, IEEE Press, New York, 1993.
29. S. Chikazumi, Physics of Ferromagnetism, 2nd ed., Oxford University Press, Oxford, 1997.
30. J.M.D. Coey, Magnetism and Magnetic Materials, Cambridge University Press, Cambridge, 2010.
31. R.C. O'Handley, Modern Magnetic Materials: Principles and Applications, Wiley, New York, 2000.
32. G. Bertotti, Hysteresis in Magnetism: For Physicists, Materials Scientists, and Engineers, Academic Press, San Diego, 1998.
33. G. Socrates, Infrared and Raman Characteristic Group Frequencies: Tables and Charts, 3rd ed., Wiley, Chichester, 2001.
34. J. Goldstein, D. Newbury, J. Michael, N. Ritchie, J. Scott, D. Joy, Scanning Electron Microscopy and X-Ray Microanalysis, 4th ed., Springer, New York, 2018.
35. D. Briggs, M.P. Seah, Practical Surface Analysis: Auger and X-Ray Photoelectron Spectroscopy, 2nd ed., Wiley, Chichester, 1990.
36. J.F. Moulder, W.F. Stickle, P.E. Sobol, K.D. Bomben, Handbook of X-Ray Photoelectron Spectroscopy, Perkin-Elmer Corporation, Minnesota, 1992.
37. A. Goldstein, et al., Scanning Electron Microscopy and X-Ray Microanalysis, 3rd ed., Springer, New York, 2003.
38. J. Coates, Interpretation of infrared spectra, a practical approach, in: R.A. Meyers (Ed.), Encyclopedia of Analytical Chemistry, Wiley, Chichester, 2000, pp. 10815–10837.
39. R. Valenzuela, Magnetic Ceramics, Cambridge University Press, Cambridge, 1994.
40. A. Goldman, Modern Ferrite Technology, 2nd ed., Springer, New York, 2006.
41. J. Ding, H. Yang, W. F. Miao, P.G. McCormick, R. Street, Nanostructured soft magnetic materials prepared by mechanical alloying, J. Alloys Compd. 281 (1998) 32–36.
42. A. Goldman, Handbook of Modern Ferromagnetic Materials, Kluwer Academic Publishers, Boston, 1999.
43. K. J. Overshott, Magnetic materials and their applications, IEE Proceedings A 127 (1980) 379–387.